Heritage Science

RESEARCH

Open Access

Clustering analysis of acoustic emission signals in the monitoring of stone monuments: case of the freeze–thaw deterioration of tuffs

Yishan Zhou[1*], Li Li[1], Yikun Liu[2], Zhongjian Zhang[3] and Toshiya Matsui[4]

Abstract

Acoustic emission (AE) technology is a promising technique for monitoring cultural monuments due to its characteristic ability to reflect status changes and perceive the development process of deterioration and damage even before their visual appearance. This study was established on the motivation of providing basic data and a methodology that can improve the signal processing, characteristics analysis and classification for the AE technique in the long-term *in-situ* monitoring of deterioration processes, starting from the freeze–thaw deterioration of tuff monuments at the Chengde site. AE monitoring was carried out with an indoor freeze–thaw deterioration experiment. As a result, a set of procedures and related methodology is proposed based on the hit-based AE waveform parameters for denoising and classification of monitored AE signals by applying hierarchical cluster analysis, k-means clustering, distribution statistics, etc. The clustering results show that some signals may indicate deterioration and signals with certain characteristics are more likely to occur at a particular deterioration phase. Signals characterized by the significant absolute energy (ABE) are presumed to be related to the propagation of cracks to the outer layer. Signals characterized by a higher indirect parameter RA (Rise time divided by peak amplitude) value may connect with the opening/closing of microcracks in the earlier phase of deterioration prior to the exposure of visible surface cracks. The peak frequency (PF) is likely to decrease as the deterioration proceeds.

Keywords Stone monuments, Tuff, Freeze–thaw deterioration, Deterioration monitoring, Acoustic emission, Cluster analysis

Introduction

Environmental and endogenous factors that affect historic monuments work together, leading to the development of the deterioration phenomenon [1]. The main objective of conservation is to stop or slow deterioration by eliminating or controlling related affecting factors. However, this is difficult to realize in practice, especially in the case of outdoor immovable heritage objects represented by stone monuments. Remedial conservation treatments, for instance, desalination, consolidation, and repairing missing parts or lacunae, can only temporarily improve the properties of monument resistance to further deterioration. Thus, it is crucial to capture the real-time dynamics of deterioration development via various monitoring methods to assess the effectiveness of conservation measurements and provide data support for their design, implementation and improvement. Nowadays, many types of *in-situ* monitoring techniques, such as displacement and strain gauges, fibre optic sensing system, thermographic imaging, etc., are being applied in the cultural heritage site. However, these methods are more adept at reflecting damage, fractures after they have

*Correspondence:
Yishan Zhou
zhouyishan@cach.org.cn
[1] China Academy of Cultural Heritage, Beijing 100029, China
[2] School of Cultural Heritage, Northwest University, Xi'an 710069, China
[3] School of Engineering and Technology, China University of Geosciences (Beijing), Beijing 100083, China
[4] Faculty of Art and Design, University of Tsukuba, Ibaraki 3050005, Japan

been revealed to the outer layer and surface. Electromagnetic detection techniques such as Ground Penetrating Radar (GPR), Magnetic Resonance Imaging (MRI), Computed Tomography (CT), X-Ray and γ-Ray detection, and ultrasonic wave measurements such as P-wave velocity testing and Ultrasonic Tomography can reveal internal disintegration. Yet the safe management of electromagnetic radiation and the portability of the instruments limit their use to status detection rather than continuous *in-situ* monitoring.

Acoustic emission (AE) technology is a promising method for monitoring physical cultural monuments subject to externally or environmentally induced loads due to its characteristic ability to reflect status changes and understand the development process of deterioration and damage even before their visual appearance. AE refers to the transient elastic wave, typically in the range of 1 kHz to 1 MHz, formed by the sudden redistribution of stored strain energy when forming a new outer surface (crack). The elastic waves propagating through the material can be recorded in real-time as electrical voltage signals by AE piezoelectric transducers positioned on the surface (Fig. 1).

To date, the AE technique has been widely used in civil, aeronautical and industrial applications as non-invasive and passive technique to assess the damage to materials and monitor the structural health of structures [2]. This technique was introduced to the conservation field in the 1980s, and related application research from various perspectives has been carried out [3]. For instance, to monitor salt crystallization in the deterioration mechanism research of masonry structures [4], the physical change in wood artifacts under environmental change can be monitored for damage risk evaluation and indoor climate management [5, 6], xylophagous insects can be detected in wooden cultural heritage musical instruments, and weathering and failure in decorative paints can be studied [7].

Although the concept of monitoring and predicting damage using AE has been proposed in 1987 [8], over these decades, some recommendations have been published to provide guidance for basic settings and procedures in practice [9, 10]. The incredible development of AE systems allows for capturing full waveforms and calculating a wide range of hit-based signal parameters (Table 1) [11, 12].

Therefore, in practice, to implement the concept for damage monitoring and prediction, the primary challenge is to accumulate a greater understanding of the correlation between the AE signals and mechanical changes. In this regard, approaches used to expound AE data to better discriminate various damage phenomena have been developed by applying direct and indirect waveform features, cumulative parameter features with time, and multivariate analysis tools, such as wavelet analysis, principal component analysis (PCA), k-means clustering, self-organizing map analysis, and artificial neural networks [11, 13, 14]. These works provide excellent inspiration for the implementation of AE in heritage conservation, but the applicability of the approach needs to be validated according to the specific requirements of different types of monuments.

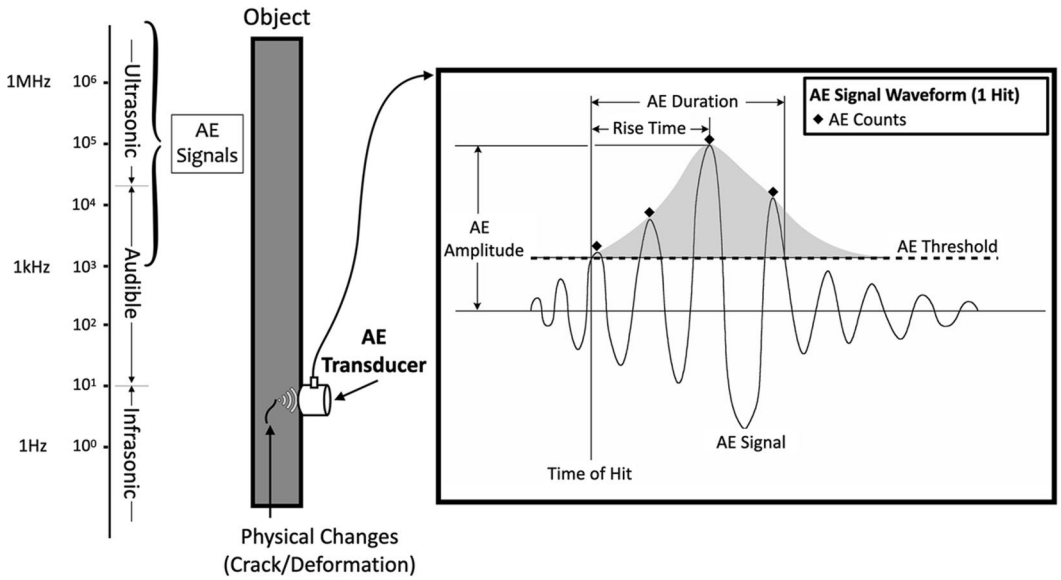

Fig. 1 The frequency range, recording scheme and related hit-based waveform parameters of AE signal

Table 1 Hit-based AE waveform parameters

AE Waveform Parameters			Code	Definition	Unit
Direct	1	Threshold	–	The predefined value such that signals with amplitude higher than which will be recorded	dB
	2	Hits	H	The AE signal exceeds threshold	–
	3	Counts	N	The number of AE signal excursions over the threshold during an AE hit	–
	4	Amplitude	A	The maximum (positive or negative) AE signal excursion during an AE hit, which indicates the magnitude of the waveform	dB
	5	Duration	D	The time between the first and last threshold crossing of an AE hit	μs
	6	Rise Time	R	The time between the first threshold crossing and the peak amplitude	μs
	7	Counts to Peak	NP	The number of AE signal excursions over the threshold between the first threshold crossing and the peak amplitude	–
	8	Absolute Energy	ABE	The integral of the squared voltage signal divided by the reference resistance (10 k-ohm) over the duration of the AE waveform packet, which is a true energy measure of the AE hit	Joules
	9	Energy	E	The integral of the rectified signal over the duration of the AE waveform packet	μVolt-sec/count
	10	Signal Strength	S		picovolt-sec
	11	Root Mean Square	RMS	An electrical engineering power term defined as the rectified time averaged AE signal, which is a measure of the continuously varying AE signal "voltage"	Volt
	12	Average Signal Level	ASL	An electrical engineering power term defined as the rectified time averaged AE signal, which is a measure of the continuously varying AE signal "amplitude"	dB
Indirect	13	Average Frequency	AF	Counts divided by Duration	kHz
	14	Reverberation Frequency	RF	The "ring down" average frequency, which is determined after the peak of the AE waveform (Counts—Counts to peak) divided by (Duration—Rise-time)	kHz
	15	Initiation Frequency	IF	The "Rise-time" average frequency, determined before the peak of the AE waveform Counts to peak divided by the rise-time	kHz
	16	Frequency Centroid	CF	The value derived from the fast Fourier transformation of the waveform associated with the AE hit, and then calculated by SUM(magnitude*frequency)/SUM(magnitude)	kHz
	17	Peak Frequency	PF	The frequency contains the largest magnitude derived from the fast Fourier transformation on the waveform associated with the AE hit	kHz
	18	RA	RA	Rise time divided by peak amplitude Useful to classify AE signals	μs/dB

This study was established on the motivation of providing basic data and a methodology that can improve the signal processing, characteristics analysis and classification for the AE technique in the long-term *in-situ* monitoring of deterioration processes, starting from typical cases.

Tuff is generally used as a collective term, referring to all volcaniclastic rocks with a volcanic matrix and varied types of grains formed by the cooling and solidification of magma. Due to its aesthetic appearance and good workability, historically, tuff has been commonly applied as construction and artwork material [1]. The best-known case in China is the Mountain Resort and its Outlying Temples, Chengde (inscribed on the World Heritage List in 1994). Most of the delicately carved statues, stela, and reliefs on the bases or railing of the architecture in this heritage site are made from tuffs quarried in the vicinity, which are called Yinwuyan (Parrot rock) by locals. According to field investigations, significant deterioration is shown by layer delamination following laminae, exfoliation, granular disintegration, discoloration and deposit (Fig. 2), especially the first one [15, 16].

According to previous investigations, the tuffs at the Chengde site show a high clay content (10–20%), and the pore size distribution in the capillary pore range (82.2%) may make the tuff far more susceptible to the presence of water [16]. *In-situ* environmental monitoring displays frequent temperature fluctuations around the freezing point in winter (November to the following January). A combination of these endogenous and environmental factors makes the prevention and continuous evolution of in situ object deterioration challenging.

Therefore, the authors decided to take the freeze–thaw deterioration of tuff monuments at the Chengde site as a starting point. AE monitoring was carried out with an indoor freeze–thaw deterioration experiment. Approaches with proven applicability to structural material in other fields [11, 13, 14], mainly k-means clustering of direct and indirect hit-based waveform parameters and other multivariate analyses, were implemented to

Fig. 2 The layer delamination and laminae deterioration phenomena of tuff monuments in Puyou Temple, Chengde: **a** base for the Buddhist statues and **b** pillar stone

challenge the characteristic analysis and classification of AE signal features occurring in different deterioration phases, and to propose some key indicative parameters of deterioration states.

Experiment setup

Freeze–thaw (F–T) deterioration experiment

From July 2020 to July 2021, the temperature data derived from the ambient environment and the surface of the outdoor pillar stone at the northwest corner of the Puyou Temple in Chengde showed that the most frequent fluctuation of 0 ℃ occurred at the beginning of winter (late November to early December) and at the end of winter (February). The greatest diurnal ambient temperature range appeared on February 4th, 2021, with a minimum of -16.1 ℃ and a maximum of 13.0 ℃ (Fig. 3).

Based on the monitoring data, the freezing stage was designed with an ambient temperature of approximately -15 ℃ by placing specimens into a temperature-controlled freezer. The thawing stage was realized by moving specimens from the freezer to a room-temperature benchtop. Each stage of freezing or thawing lasted two hours.

To simulate water transport between the stone monuments and the foundation materials under them, the experiment was designed with reference to the water absorption coefficient tests [17]. The specimens were set in the direction perpendicular to the bedding (with side A as the bottom side) on the water-saturated high-density foam layers. The piezoelectric AE transducers were set on side B of the specimens, which was taken as the main observation surface (Fig. 4). A thermocouple temperature sensor equipped with an Onset UX120-014 M temperature recorder was attached on side E of each specimen to obtain the surface temperature every minute.

According to the percentile curves of the surface temperature data within each cycle shown in Fig. 5b, cyclic variation between the freezing and thawing stages was achieved as the experimental design. The box frame indicates that the temperature drops to a low point of around 0 ℃ approximately 50 min after the start of a freezing stage and then remains steady. Upon entering the thawing stage, the temperature first escalates to around 1 °C, remains there for approximately 30 min, and then climbs toward room temperature.

In addition, time-lapse photography equipment (ATLI EON TS T100, 1 min shooting interval) was set to record real-time changes during the experiment to eliminate some noise signals caused by transducer detachment and artificial interference.

Materials and specimens

The tuff sampled in an abandoned quarry around the Chengde site was used in this study. Three cubic specimens (CD-FT-1/2/3) with a 50 mm edge size were cut in the direction perpendicular to the horizontal bedding. The four sides perpendicular to the bedding were labeled A, B, C and D, and the remaining horizontal sides were labeled E and F.

Results of mineralogical composition analysis of X-ray fluorescence (XRF, Epsilon 4, Malvern Panalytical Ltd., UK) and X-ray differaction (XRD, SmartLab, Rigaku corporation, JP, CuK α radiation, 40 mV/150 mA, 0.02 s/step) shows the tuff specimens mainly consist of silica (about 74%) and alumina (about 19%). The mineral compositions indicate the most significant SiO_2 content of about 70%, followed by about 24% clay minerals (primary kaolinite), and about 2% K-feldspar and hematite respectively (Table 2). The examination by polarised light microscope shows that the specimens are mainly constituted of phenocryst (5–10%) and matrix (85–90%), with fewer amounts of vitroclastic (about 5%) (Fig. 6). Phenocryst consists mainly of plagioclase, a little quartz, and some isolated biotite, with grain sizes from 0.25 to 0.80 mm. Plagioclases are in the form of prism or plate.

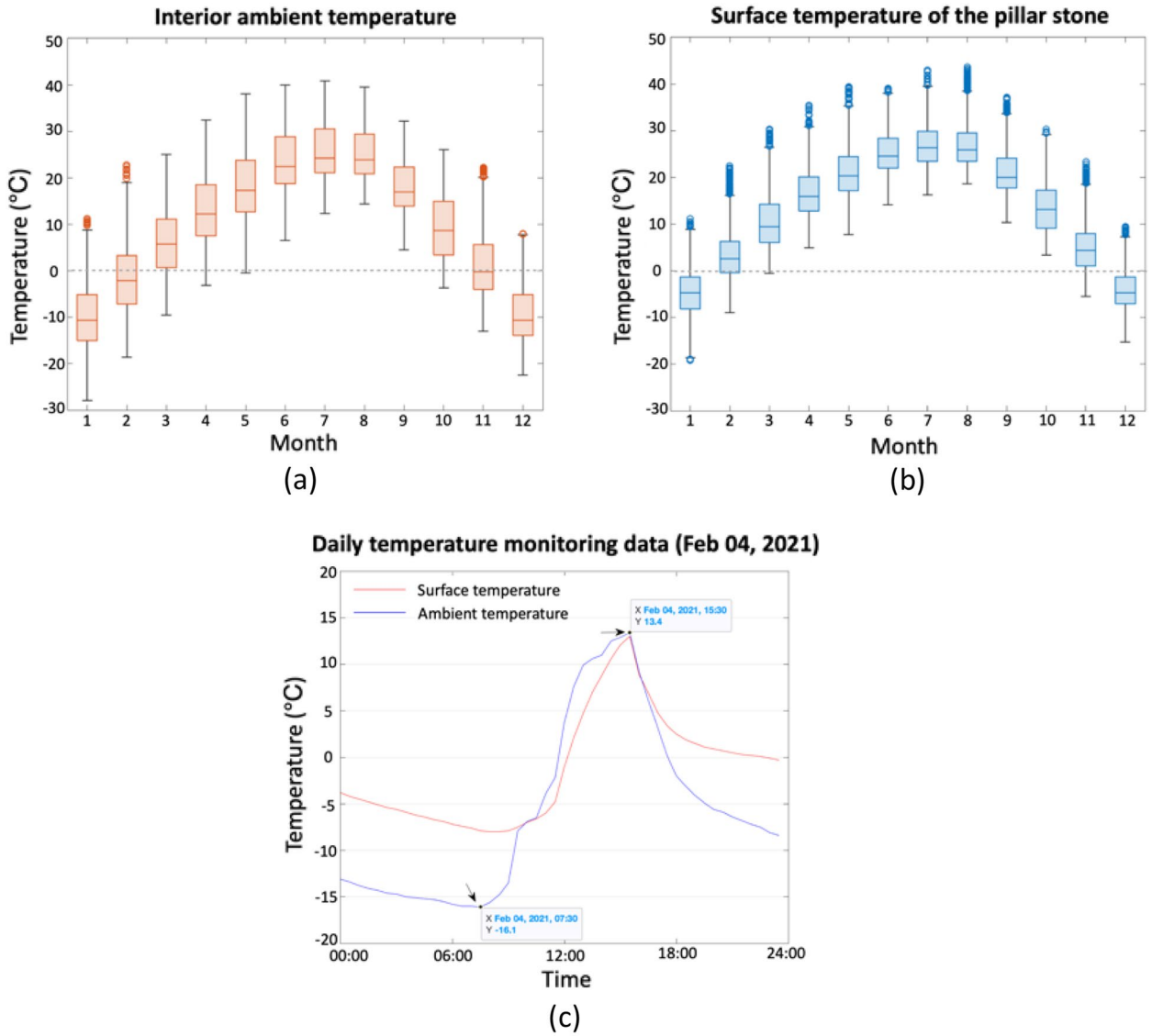

Fig. 3 The temperature data monitored from July 2020 to July 2021 for the outdoor pillar stone at the northwest corner of the Puyou Temple in Chengde. **a** Ambient temperature, **b** surface temperature, and **c** ambient temperature with the greatest diurnal on February 4th, 2021

Matrix mainly contains plagioclase, also a little quartz. Grain sizes of the matrix range from 0.05 to 0.08 mm.

Evaluation of deterioration

According to a literature survey, for tuffs, the value of the effective porosity increases and the value of P-wave velocity decreases with an increase in the number of F–T cycles [18].

In this study, after every 5th F–T cycle, the deterioration of specimens was evaluated via microscopic observation, water absorption coefficient testing and P-wave velocity testing until 90 cycles were performed and all three specimens were severely damaged.

A Keyence VHX-2000 digital microscope system, equipped with the VH-Z20R ultracompact high-performance zoom lens, was used to observe fracture development on the surface of specimens at 30 – 100 × magnification.

The capillary water absorption test was performed with reference to the ISO 15148:2002/Amd 1:2016 standard [17]. The specimens were immersed in deionized water with side A facing downward, the water level of immersion was kept at 5 mm during the test, and the changes in specimen mass were recorded at intervals of 1 min, 5 min, 10 min, 15 min, 30 min, 1 h, 2 h, 4 h, and 24 h after the start of immersion. The change in mass was

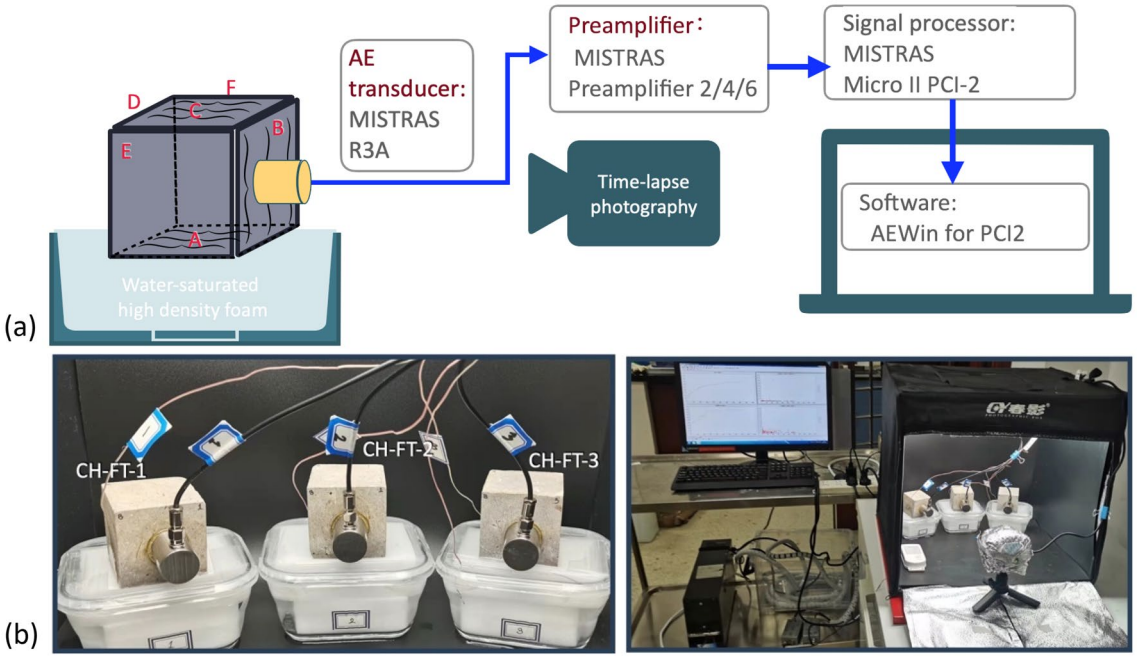

Fig. 4 The scheme of F–T deterioration. **a** AE monitoring system and **b** status of the specimens during the thawing stage

One ***Freeze-Thaw*** cycle (4h)		
Stage	Freeze	Thaw
Duration (h)	2	2
T (°C)	-15	Room temperature

(a)

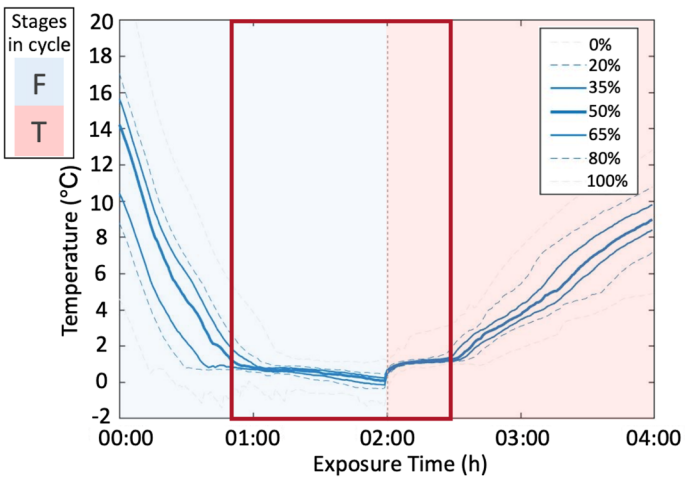

(b)

Fig. 5 **a** F–T cycle of the deterioration experiment and **b** percentile curves of the surface temperature data within each F–T cycle

Table 2 Results of mineralogical composition analysis (XRF and XRD)

Specimen	Major oxide element (Wt%)					Mineralogical composition (Wt%)						Percentage of clay minerals(Wt%)	
	SiO_2	Al_2O_3	K_2O	Fe_2O_3	Others	Quartz	K-feldspar	Albite	Dolomite	Hematite	Clay minerals	Illite	Kaolinite
CD-FT-1	74.9	18.6	2.9	2.1	1.5	70.4	2.4	0.1	0.6	2.1	24.4	5.0	95.0
CD-FT-2	73.8	18.6	2.8	2.4	2.3	72.0	2.7	0.4	0.7	1.1	23.1	3.0	97.0
CD-FT-3	74.8	19.0	2.7	1.8	1.8	70.8	2.7	0.1	0.8	1.4	24.2	1.0	99.0

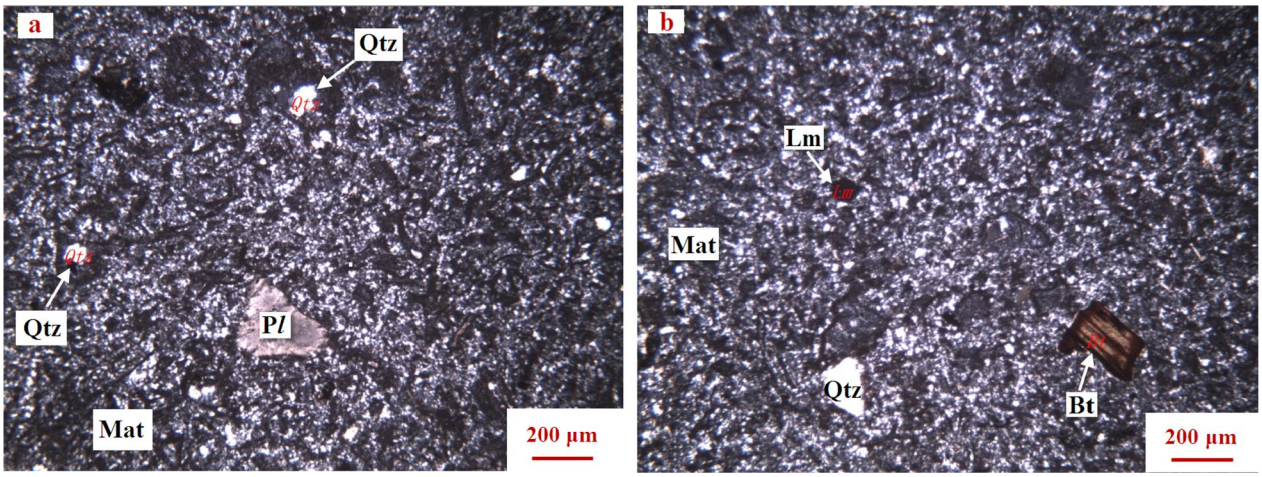

Fig. 6 Image **a** and **b** obtained by optical microscope. Qtz-Quartz, Pl-Plagioclase, Bt-Biotite, Lm-limonite, Mat-Matrix

plotted versus the square root of the corresponding time, and linear regression was performed on the linear part of the curve to obtain the slope as the corresponding coefficient.

The P-wave velocity test was performed using Pundit 250 (Proceq AG, CH) with 54 kHz transducers using the pulse transmission technique. For each specimen, the test was both along and perpendicular to the bedding (the transmitter and receiver positioned on the opposite B-D and E–F sides). The test surface was divided into 9 equal squares and tested to calculate the mean and standard deviation values.

AE monitoring system and signal analysis methods

AE monitoring was conducted continuously during each cycle, except for the process of moving specimens into thawing conditions where the instrument was paused to avoid recording interfering signals. One AE transducer was attached on side B of each specimen with a polyamide-based hot melt adhesive (8620N, SUNTIP, Inc., PRC), which has a lower glass transition temperature of − 40 °C, ensuring that the transducer subject to the frequent F–T cycles of this experiment remains mounted firmly.

A multichannel unit Micro II PCI-2 equipped with Preamplifier 2/4/6 and AE transducer R3A (MISTRAS Group Inc., USA) was applied with the following input parameters: a preamplifier total gain of 40 dB, a threshold of 36 dB, a sampling frequency of 1 MSPS (1 million times per second), a high-pass filter and low-pass filter of 1 kHz and 1 MHz, respectively, and a peak definition time (PDT)/hit definition time (HDT)/hit lock-out time (HLT) of 300/600/1000 (μs).

The characteristics analysis and classification of the AE signals in the F–T degradation stages was performed with the hit-based waveform parameters listed in Table 1 using the following analysis methods with MATLAB R2021a (MathWorks, Inc., USA). The procedures of AE signal analysis were shown in Fig. 7.

Denoising process with indirect waveform parameters

It has been proven that AE signals with long duration (D), larger count (N) and low amplitude (A) are recorded during plastic deformation, while signals with shorter D, smaller N and higher A are recorded during brittle fracture [19]. Therefore, the indirect parameter RA value and average frequency (AF), which are ratios of the waveform-related direct parameters, are proposed for signal discrimination. Previous studies have demonstrated their effectiveness. AE events characterized by high AF and low RA values can be correlated to tensile crack propagation. Alternatively, AE signals characterized by high RA and low AF values identify other types of cracks, such as shear crack propagation (Fig. 8) [20]. In this study, the RA value and AF were applied for the preliminary denoising process by determining outlier signals detached from the main signals.

Hierarchical cluster analysis [21, 22]

Hierarchical cluster analysis utilizes an algorithm for clustering data by creating a cluster tree with a multilevel hierarchy. This algorithm starts by treating each observation as a separate cluster. Then, it repeatedly executes the following two steps: calculate the distance between every pair of clusters and then merge the pairs of clusters that are in close proximity. This iterative process continues until all the clusters are merged together.

In this study, hierarchical cluster analysis was performed for two purposes:

A) To exhibit the correlation level among the various AE parameters. Thus, when choosing the most repre-

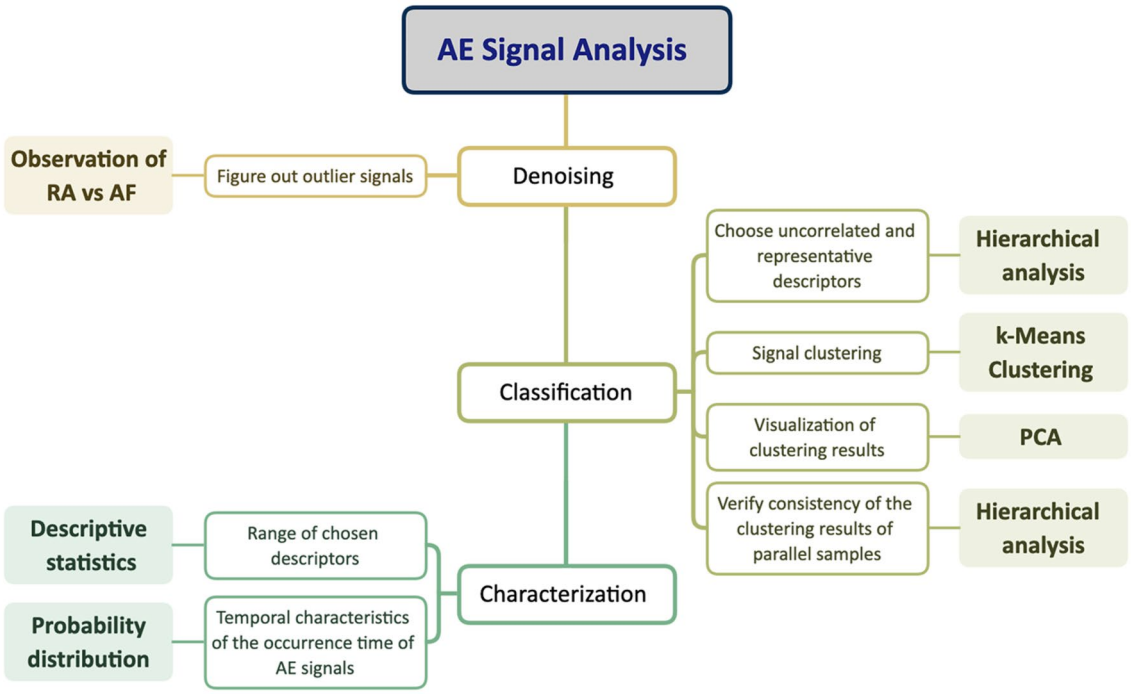

Fig. 7 Scheme of procedures for AE signal analysis

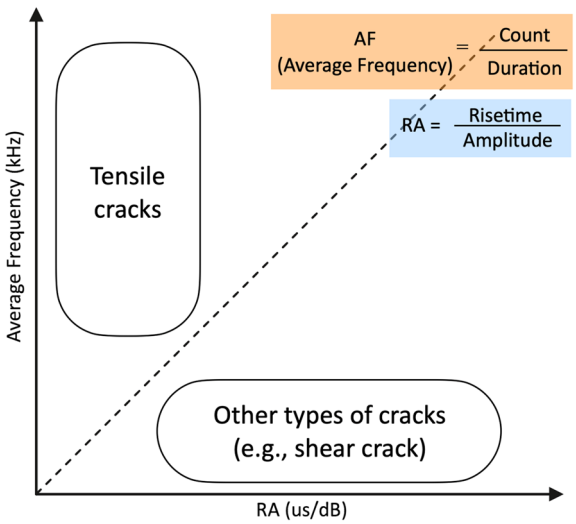

Fig. 8 Signal discrimination according to indirect parameters RA vs. AF

sentative descriptors for the following work of signal clustering, the correlated and consequently redundant descriptors could be eliminated.

B) To verify the consistency of the clustering results among the three specimens. The values in the dataset were normalized with the z score formula before clustering. The pairwise distance between pairs of observations was calculated with the correlation distance metric, and the cluster tree was created with the average method for calculating the distance between clusters.

K-means clustering [23, 24]

The classification of denoised AE signals was performed using k-means clustering with the normalized dataset of the selected parameters.

The k-means clustering method is a partition method that allows obtaining a nonsupervised classification by data features. "k-means" refers to a process that mainly performs two tasks: determine the best value for "k-number" centroids and iteratively assign each data point to its closest k-center until each data point belongs to the cluster with the nearest "mean" cluster center.

In this study, the silhouette method was applied to determine the optimal k-number that corresponds to the solution with the highest silhouette criterion value. K-means clustering was performed using the squared euclidean distance metric.

Principal component analysis [25]

The classification result was visualized using principal component analysis (PCA), which could reduce the dimension of the data. PCA is a type of multivariate analysis generally applied to determine the similarities and

differences in a dataset. Its basic concept is to simplify a dataset with multiple variables into a smaller number of uncorrelated new variables, which still contain most of the information of the original dataset.

Probability distribution

The probability distribution is an idealized frequency distribution representing the number of times each possible value of a variable occurs in the dataset.

In this study, the temporal characteristics of the occurrence time of AE signals were depicted with the probability density function for the normal kernel distribution; this function was fit to the occurrence stages within a single cycle and the occurrence phases during the overall deterioration process.

Results and discussion

Deterioration development and stages

The deterioration development of CD-FT-1/2 is relatively similar in the three specimens. Few microcracks with micron-sized widths were observed under microscopic observation following the first 5 F–T cycles. No other visible surface cracks developed until after 50 cycles. After 70 cycles, new cracks appeared and developed rapidly, accompanied by the opening of existing cracks, and after 85 cycles, cracks crossed completely through and split the specimens. In contrast, the deterioration development of CD-FT-3 was not apparent in the early stage until after 50 cycles when a crack with a micron-sized width was observed in the lower left corner of the B surface (Figs. 9 and 10). However, after 56 cycles the crack developed rapidly along with some newly revealed cracks and soon after 62 cycles the first revealed crack crossed through and split the specimen. Then, after 70 cycles, the lower part of the specimen was largely fragmented by multiple cracks.

The macroscopic morphological change process of the three specimens is reflected in the P-wave velocity test results. As shown in Table 3, the P-wave velocity measured after certain F-T cycles of all specimens decreased with exposed F–T cycles. And the stepped declines could be seen in the boxplot (Fig. 11a) of P-wave velocity changes taken as a percentage of the initial value.

Compared to the initial values, both along (∥) and perpendicular (⊥)to the bedding direction, the latter value was greater. For CD-FT-1/2, significant declines were observed after 5, 70 and 75 cycles, and the ranges between the maximum-minimum value of the percentage changes gradually increased after 70 cycles. For the more rapidly deteriorated CD-FT-3, the specimen was too fragmented to test after 70 cycles, so only the changes in P-wave velocity after 50 cycles were present. A noticeable decline was observed after 5 and 50 cycles. The significant decline in P-wave velocity reflects the formation of more microcracks, the opening of existing microcracks or the increase in local variations in the specimen due to the locally occurring deterioration in

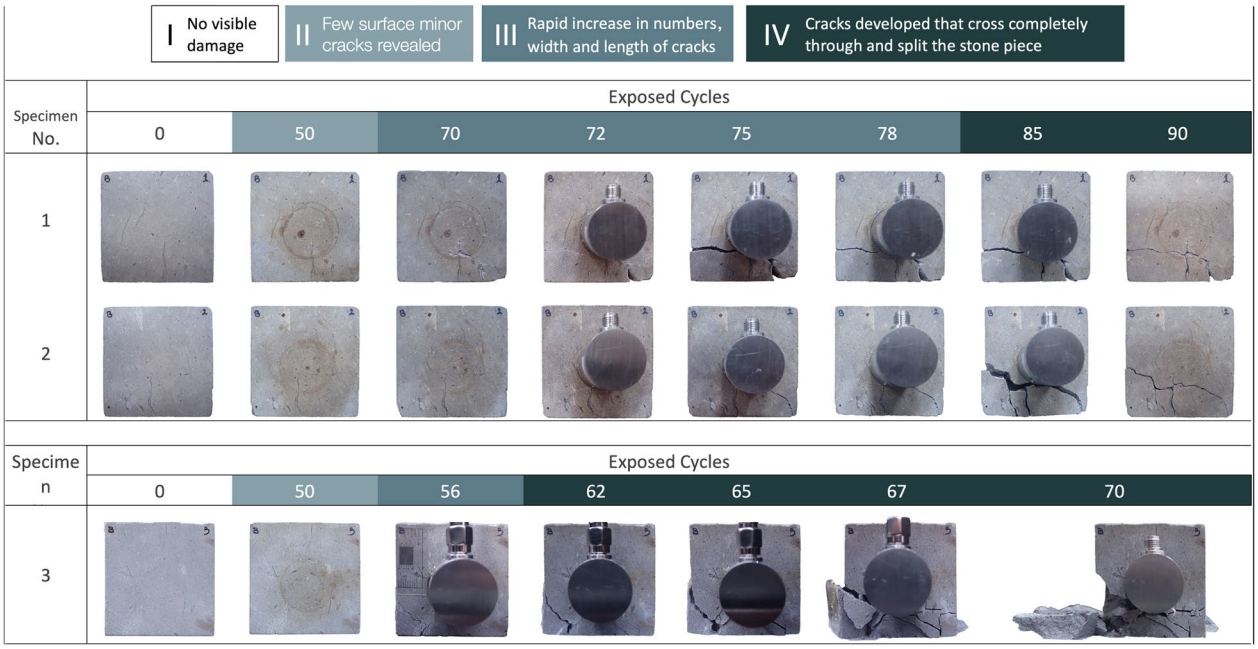

Fig. 9 Macromorphological changes on the B-side of the specimen throughout the F–T deterioration process

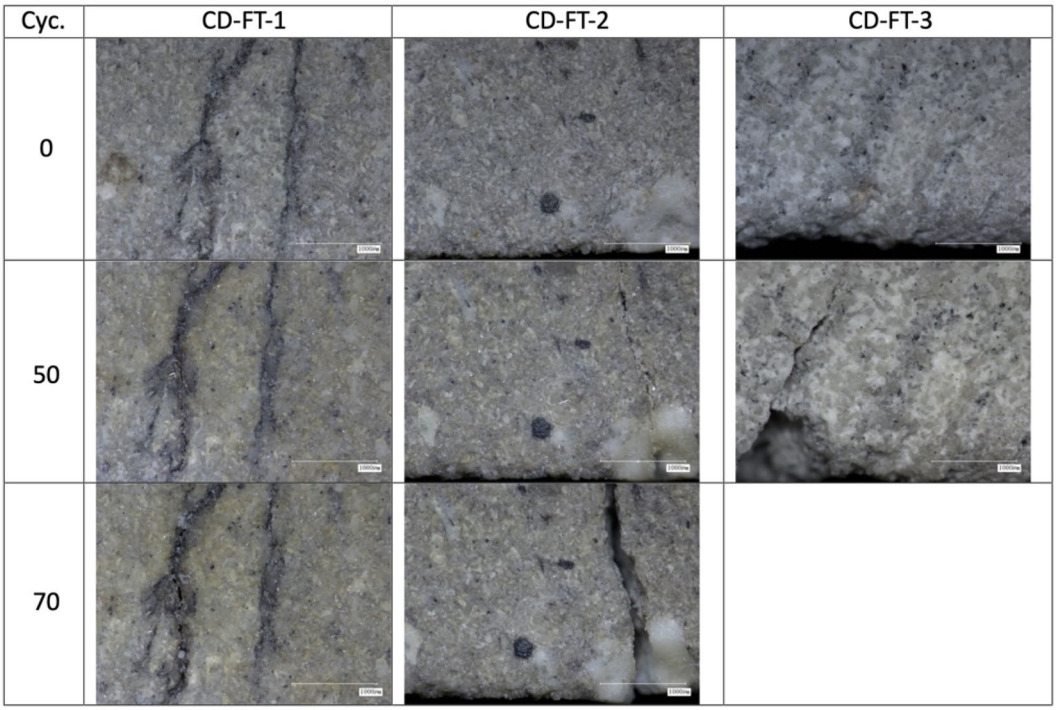

Fig. 10 Microscopic observation(100x) of specimens in the overall F–T deterioration process

the lower half of the specimens under the F–T experimental design applied in this study.

The capillary water absorption test could not be performed throughout the F–T experiment due to the fragmentation of the specimens in the latter stage of the experiment. While the obtained capillary water absorption coefficients indicate a higher water absorption capacity of CD-FT-3 compared to CD-FT-1/2 (Table 3). This may be the critical factor in the more rapid deterioration of CD-FT-3, as water content is a major control of freeze–thaw deterioration [26]. While no pronounced decreasing or increasing trend with exposed F-T cycles could be observed in the case of these three specimens from Fig. 11b. Water absorption due to capillary action is determined by the balance between the fluid's surface capillary pressure and its gravity pressure, and the capillary pressure increases with decreasing capillary diameter of pores in a material [27]. The change in porosity and its distribution, along with the development of microcracks in tuff, can influence its capillary water absorbability. Thus, capillary water absorption coefficients may not be a suitable indicator of deterioration development in this study.

According to macroscopic morphological change and P-wave velocity test results, the surface deterioration of the specimens can be divided into four phases during the whole F–T deterioration process, as shown in the following and Table 4:

Phase I: No visible damage on the surface.

Phase II: Few minor cracks were revealed on the surface with micron-sized widths.

Phase III: Rapid increase in the number, width and length of cracks.

Phase IV: Cracks developed that cross completely through and split the stone piece.

AE signal analysis

Denoising

Based on a preliminary test, the threshold was set as 36 dB to guarantee that environmental noise was eliminated. The RA value (x-axis), AF(z-axis) and the number of F–T deterioration cycles when the signal was acquired (y-axis) were displayed as a 3D scatter plot in Fig. 12, with data driven color mapping according to the occurrence time of each signal in the corresponding F–T deterioration cycle from purple to yellow. The freezing stage is 0–7200 s and presents as purple to blue, and the thawing stage is 7200–14,400 s and presents as green to yellow.

Figure 12 shows that the primary signal ranges in the RA value and AF are 0–200 μs/dB and 0–3000 kHz, respectively. In the plot of CD-FT-1/2, sequences of purplish abnormal signals with RA values over 200 are

Table 3 Results of P-wave velocity and water absorption coefficient test

Exposed F–T cycles	CD-FT-1					CD-FT-2					CD-FT-3				
	P-wave velocity (m/s)				capillary water absorption coefficient ($kg/m^2/h^{0.5}$)	P-wave velocity (m/s)				capillary water absorption coefficient ($kg/m^2/h^{0.5}$)	P-wave velocity (m/s)				capillary water absorption coefficient ($kg/m^2/h^{0.5}$)
	∥		⊥			∥		⊥			∥		⊥		
	μ	σ	μ	σ		μ	σ	μ	σ		μ	σ	μ	σ	
0	1420.3	134.9	1166.1	106.4	2.06	1430.1	141.2	1168.6	100.4	2.14	1360.6	122.2	1385.1	103.1	2.93
5	1315.0	103.4	1196.3	197.2	1.96	1344.0	149.7	1138.5	165.3	2.21	1268.3	22.2	1352.3	127.5	2.86
10	1284.7	22.9	1200.9	196.3	1.94	1319.9	99.8	1146.6	143.6	2.08	1267.6	24.3	1350.3	121.2	2.84
20	1295.6	17.5	1207.7	190.3	1.94	1316.9	92.9	1130.9	164.7	2.03	1258.6	21.6	1348.0	125.5	2.68
30	1298.2	16.9	1214.8	187.8	1.98	1328.8	100.5	1137.8	166.4	2.03	1271.3	14.2	1348.1	127.1	2.82
50	1296.7	15.7	1200.0	189.9	2.13	1299.8	122.1	1087.1	194.3	2.08	1249.0	27.7	1266.4	187.7	3.27
70	1123.3	124.6	1095.7	285.4		1101.8	364.8	912.0	292.4						
72	1131.3	133.4	1066.4	278.3		1087.0	333.1	869.9	298.0						
75	1045.1	241.7	1050.1	268.6		1025.4	279.8	853.5	288.8						
78	1018.0	293.8	987.2	286.7		1065.8	313.8	820.4	306.0						
85	1024.3	299.8	968.0	294.1		1040.6	325.9	678.0	436.4						

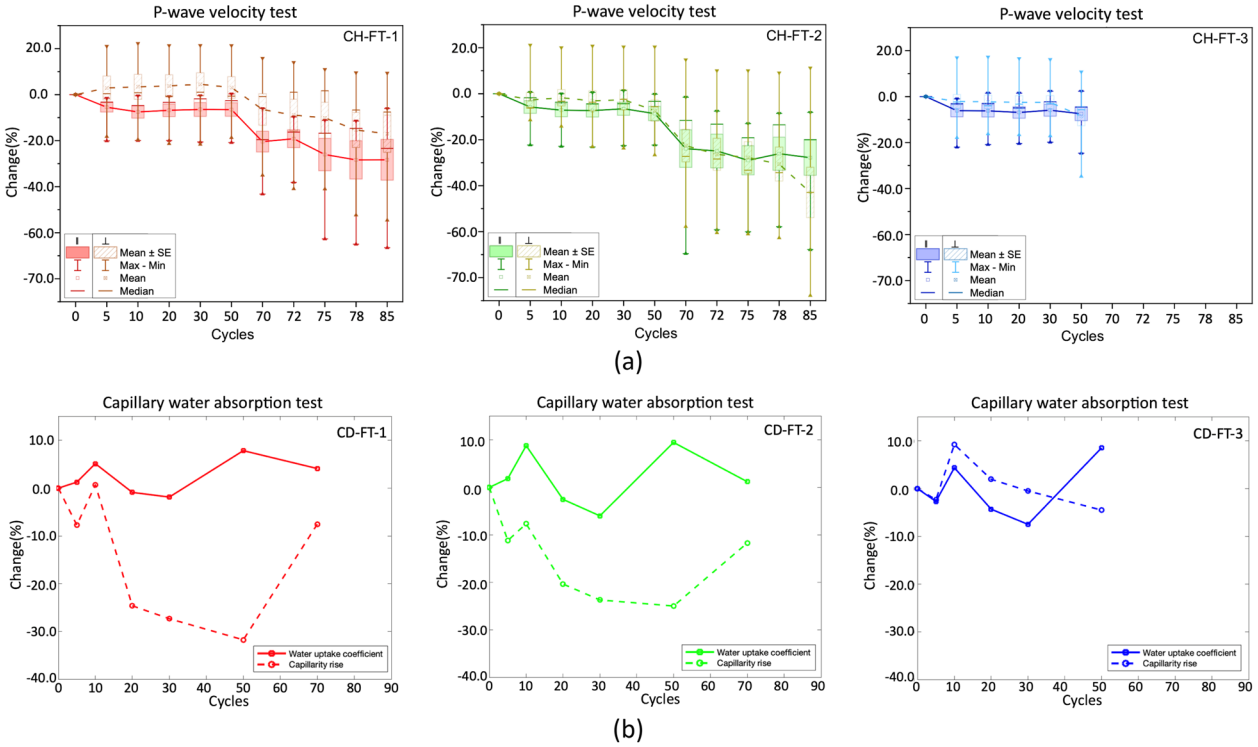

Fig. 11 Changes in and P-wave velocity **a** and capillary absorption **b** of the specimens throughout the F–T deterioration process

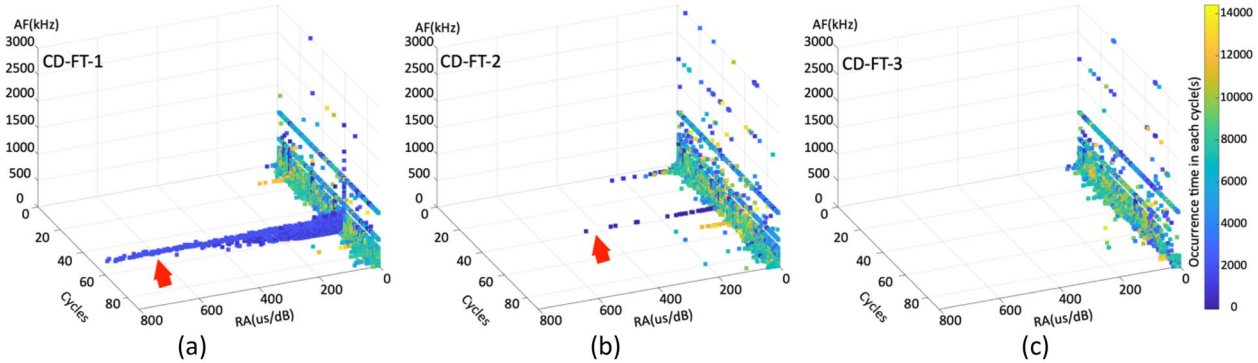

Fig. 12 The 3D scatter plot of RA vs. cycles vs. AF of each specimen Data point color mapping according to the occurrence time in each signal in the corresponding exposed cycle, **a** CD-FT-1, **b** CD-FT-2, **c** CD-FT-3

present. The abnormal signals of CD-FT-1 occurred in the freezing stage of the 59th cycle, which are presumed to be electrical noise signals caused by loose contact with the transducer wire. Abnormal signals of CD-FT-2 appeared within the first few hundred seconds of the 4th and 38th cycles, which are likely generated due to the unstable specimens status or the instrument connection cable at the beginning of cycles. Further analyses were performed after removing the abnormal signals.

Classification

As shown in Table 1, the various kinds of direct and indirect AE parameters could be roughly divided into waveform-, strength- and frequency-related groups according to their definitions. The RA value and AF which are correlated with 2 kinds of waveform-related parameters

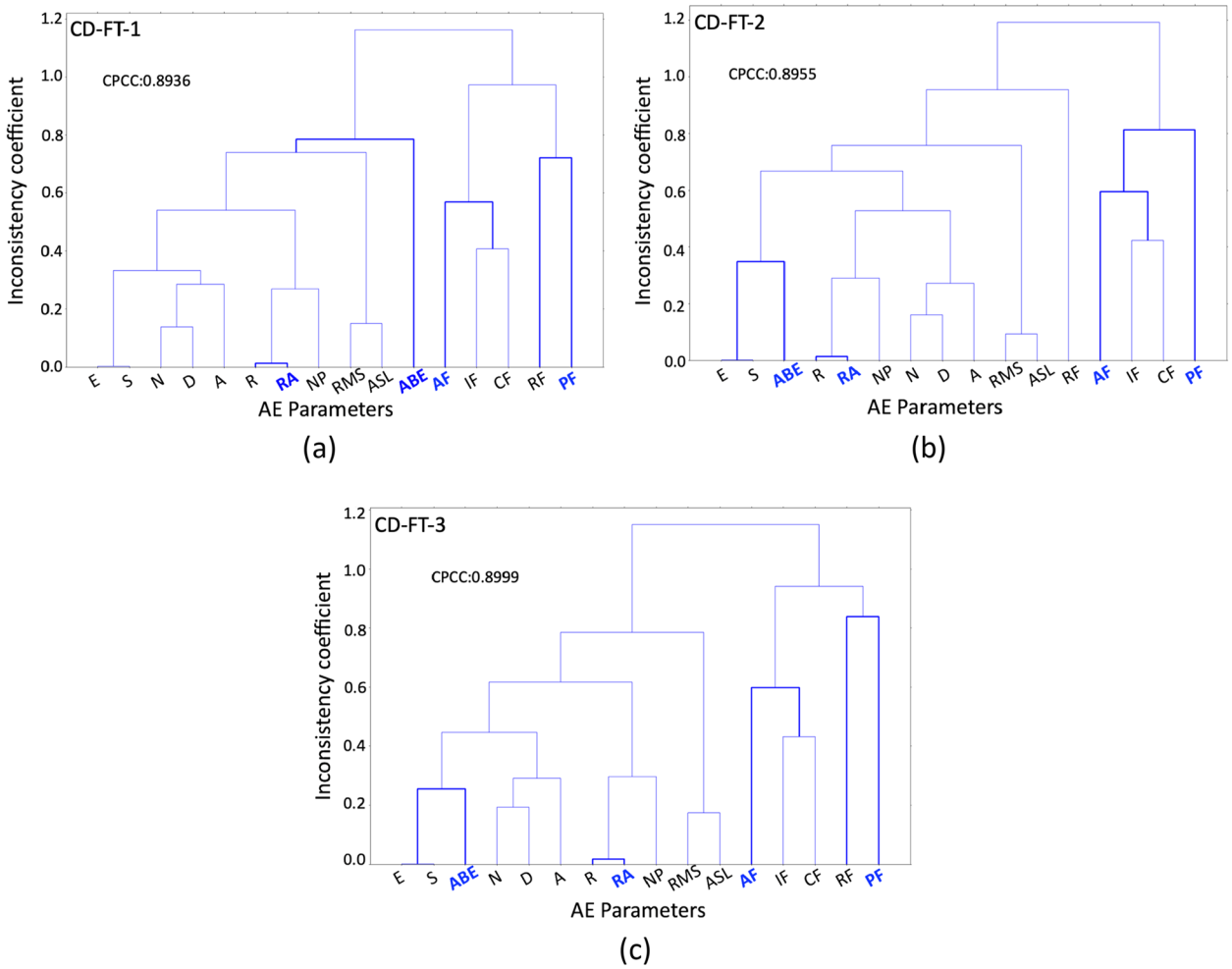

Fig. 13 Hierarchical analyses with 16 AE parameters for each specimen to evaluate the correlation level among the parameters, **a** CD-FT-1, **b** CD-FT-2, **c** CD-FT-3

respectively (R and A for RA, N and D for AF), along with strength-related parameter ABE and frequency-related parameter PF were selected for the following analyses. The dendrograms (Fig. 13) obtained by hierarchical analysis with 16 AE parameters of each specimen in the overall F–T cycles show parameters linked by U-shaped lines. The height of U-shaped links indicates the correlation between parameters. The greater the difference in height, the greater the dissimilarity. The heights of the links among the RA value, AF, ABE and PF are all significantly different in the case of the three specimens. This verifies that these four parameters are likely providing information about signals from different aspects.

The denoised AE signals were clustered into 7 clusters using the normalized dataset of the selected parameters, namely, RA value, AF, ABE and PF, with the k-means clustering algorithm, based on optimal cluster number evaluation results.

The scatter plots of the PC1 and PC3 scores, obtained from PCA, with data point color mapping according to cluster indices, were used to visualize the clustering results (Fig. 14). The asterisks characterize the PCA loadings of the four selected parameters, that is, their contribution values in the PC1 and PC3 scores.

As shown in Fig. 13, if one views an axis between the asterisks representing the RA value and AF loadings, then it is clear that the clusters are distributed approximately along this axis. Cluster (Clu.) 7 in red is distributed closest to the RA value loading side, while Clu. 1 in pink is distributed closest to the AF loading side. If one views the asterisk between the ABE and PF loads as another axis, then Clu. 4 in dark green is distributed closest to the ABE loading side, while Clu. 2 in dark blue is distributed closer to the PF loading side. From this, it is then possible to roughly define the most representative

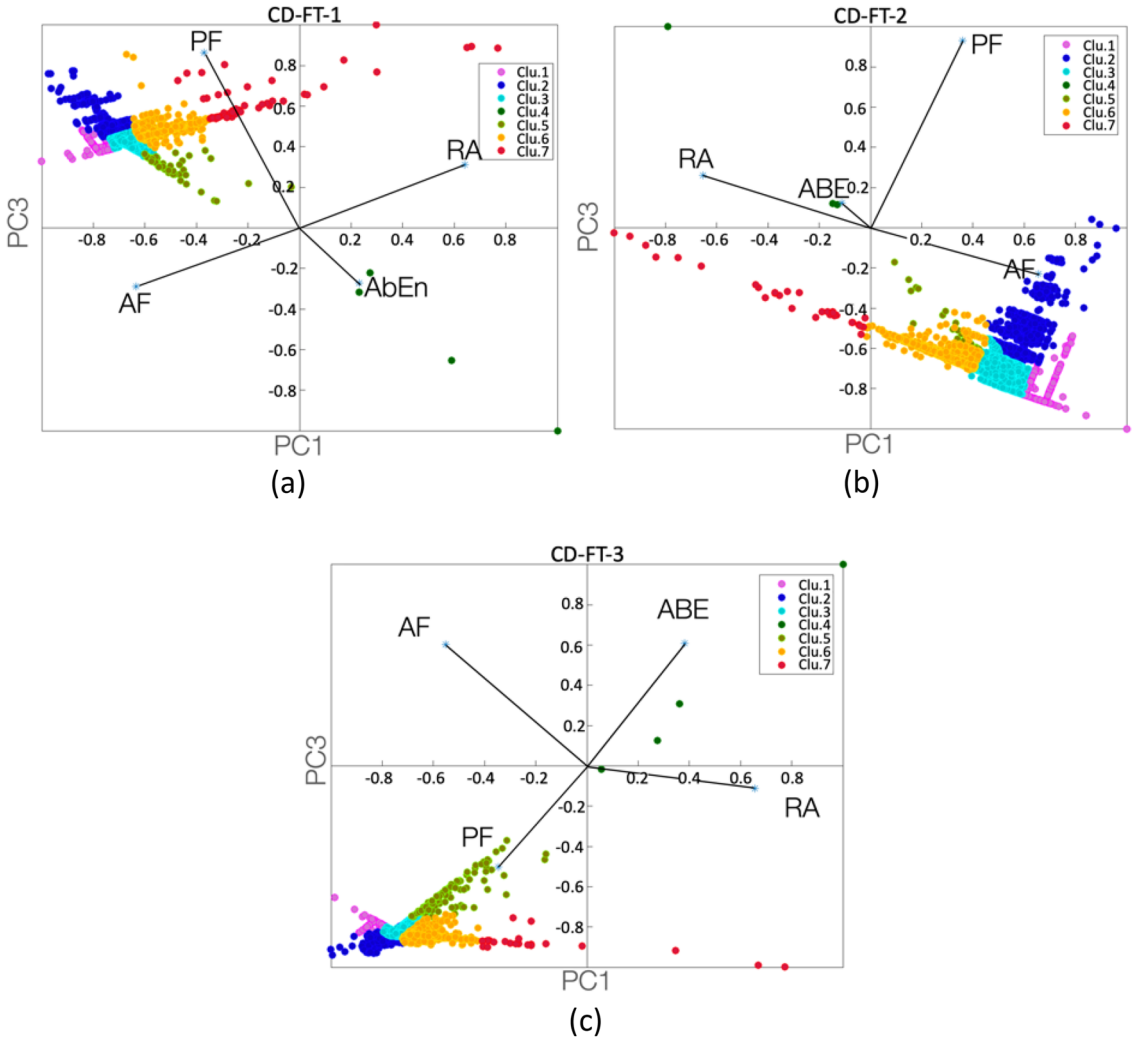

Fig. 14 The scatter plots of the PC1 and PC3 scores obtained from PCA of each specimen, **a** CD-FT-1, **b** CD-FT-2, **c** CD-FT-3

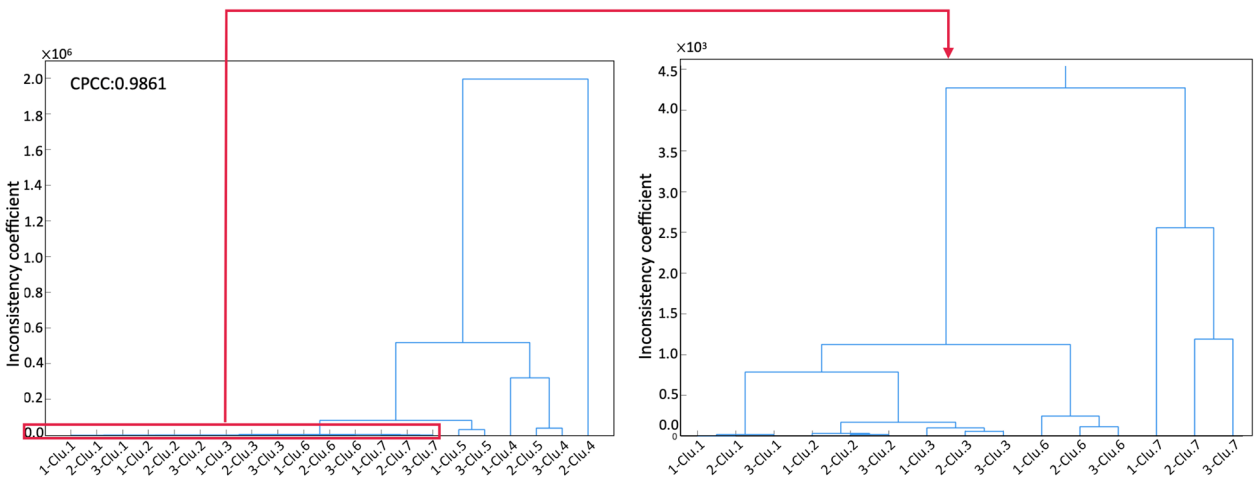

Fig. 15 Hierarchical analysis with clustering result of the three specimens

Table 4 Phases of deterioration

Phases of deterioration	Exposed cycles		
	CD-FT-1	CD-FT-2	CD-FT-3
I	–		0–30
II	0–50		31–56
III	51–78		57–62
IV	79–90		63–90

parameter among the clusters, namely, AF for Clu. 1, PF for Clu. 2, ABE for Clu. 4, and RA for Clu. 7.

To verify the consistency of the clustering results among the three specimens, the cluster's correlation level was displayed using hierarchical cluster analysis with the mean value of each cluster. The dendrogram (Fig. 15) falls into two groups that are connected by links at a much higher level in the tree. The right group contains only 2-Clu.4 (Clu. 4 of CD-FT-2). Clu.1/2/3/6/7 of the three specimens fall into a group connected by a link at a much lower level, as framed in the dendrogram, compared with the other groups containing Clu. 4/5.

The enlarged area in the frame shows that Clu. 1/2/3/6/7 are all clustered into five groups along with the corresponding clusters of the three specimens. The heights of the links among these five groups imply the higher inconsistency of Clu. 6 and 7 with Clu. 1, 2 and 3. Clu. 4/5 fall into groups connected by links at a much higher level on the right side of the tree, indicating significant inconsistency with the other clusters, and are grouped together in the following discussion.

Characterization

The minimum, 1st percentile, median, 3rd percentile and maximum values of the selected parameters in Table 5 present the range characteristics of each cluster. Regardless of the specimen, the RA values for the Clu. 1 to Clu. 7 clusters ranged from low to high, and the AF ranged from high to low. However, Clu. 2 exhibited the greatest PF with the broadest distribution, and Clu. 4 and Clu. 5 exhibited (Table 5) distinctively greater ABEs. This is consistent with previous observations based on PCA.

The probability distribution for monitored AE signals within a single cycle in Fig. 16 shows the dominant peak at the beginning of the thawing stage. Except for Clu. 1, 2 and 3, the distribution of some clusters shows distinctively different distribution characteristics. Clu. 4 and 5 show bimodal unequal distributions with one significant peak in the 2nd hour of the freezing stage and one minor peak at the beginning of the thawing stage. Clu. 6 shows multimodal distributions with the dominant peaks in the 2nd hour of the freezing stage. Clu. 7 shows wider multimodal distributions with some minor peaks over the whole F–T cycle, while in the thawing stage, it could be roughly described as bimodal distributions with higher peaks at the very beginning phase and the 2nd hour of the thawing stage.

Although the deterioration process of CD-FT-3 is significantly more accelerated than that of CD-FT-1/2, the

Table 5 The descriptive statics for the clustering results

Clu.	Spec.	RA					AF					PF					ABE				
		Min	Q1	Median	Q3	MAX	Min	Q1	Median	Q3	MAX	Min	Q1	Median	Q3	MAX	Min	Q1	Median	Q3	MAX
1	1	0.00	0.00	0.00	0.03	0.18	429	500	1000	1000	3000	13	19	21	27	143	2.53E-01	5.32E-01	7.31E-01	9.99E-01	3.68E+00
	2	0.00	0.03	0.29	0.88	10.74	0	32	53	73	1000	66	92	96	127	452	0.00E+00	4.14E+00	1.31E+01	4.48E+01	5.99E+04
	3	0.00	0.00	0.00	0.03	0.18	500	500	1000	1000	1500	11	18	23	36	175	1.72E-01	5.15E-01	7.05E-01	9.77E-01	8.13E+00
2	1	0.00	0.05	0.26	0.72	9.73	0	43	63	83	1000	60	90	95	101	495	0.00E+00	4.22E+00	1.28E+01	4.96E+01	3.43E+04
	2	0.00	0.03	0.28	0.87	10.74	0	31	53	74	1000	60	92	96	127	452	0.00E+00	4.12E+00	1.30E+01	4.46E+01	5.99E+04
	3	0.00	0.05	0.28	0.74	7.64	0	36	53	71	1167	56	65	93	99	489	0.00E+00	4.70E+00	1.44E+01	5.36E+01	3.13E+04
3	1	0.00	0.15	0.56	1.33	6.55	0	23	31	45	400	10	19	20	25	65	0.00E+00	8.93E+00	3.18E+01	1.18E+02	4.95E+04
	2	0.00	0.19	0.60	1.40	9.49	0	20	27	41	400	1	19	23	24	99	0.00E+00	9.88E+00	3.70E+01	1.37E+02	2.05E+05
	3	0.00	0.10	0.49	0.98	5.31	0	22	32	49	400	8	18	20	24	59	0.00E+00	7.52E+00	2.55E+01	1.01E+02	3.40E+04
4 & 5	1	0.00	0.51	0.90	3.08	27.34	0	20	22	26	45	18	19	20	22	51	5.10E+04	7.09E+04	9.13E+04	1.24E+05	1.07E+06
	2	0.27	0.54	0.64	0.99	18.11	16	19	21	23	34	18	19	19	23	29	2.36E+05	2.66E+05	3.72E+05	7.55E+05	3.13E+06
	3	0.00	0.49	1.27	3.63	22.85	0	18	24	27	73	15	18	20	25	100	3.47E+04	4.60E+04	6.26E+04	8.79E+04	6.19E+05
6	1	6.49	8.54	11.10	14.50	32.86	2	10	14	18	38	10	20	21	26	483	5.74E+00	7.12E+01	2.02E+02	6.39E+02	5.11E+04
	2	9.49	11.24	13.63	16.73	38.78	2	10	14	18	64	1	20	23	26	140	3.25E+00	9.50E+01	2.44E+02	8.26E+02	1.72E+05
	3	5.03	6.53	8.85	11.44	31.93	2	12	16	19	77	12	16	19	24	132	6.81E+00	7.55E+01	1.90E+02	6.58E+02	3.60E+04
7	1	32.36	38.32	42.19	54.82	139.77	4	10	13	16	27	11	20	21.5	44	295	7.76E+00	1.79E+02	6.31E+02	3.36E+03	2.51E+04
	2	39.95	47.33	51.32	67.33	108.72	5	8	12	17	25	15	18	19	21	41	2.11E+02	4.90E+02	8.80E+02	6.09E+03	4.12E+04
	3	33.89	38.15	45.76	52.43	148.88	3	11	14	16	26	14	17	20	28	95	1.90E+02	6.32E+02	1.51E+03	4.17E+03	3.93E+04

Low Moderate High Q1: 25th percentile Q3: 75th percentile

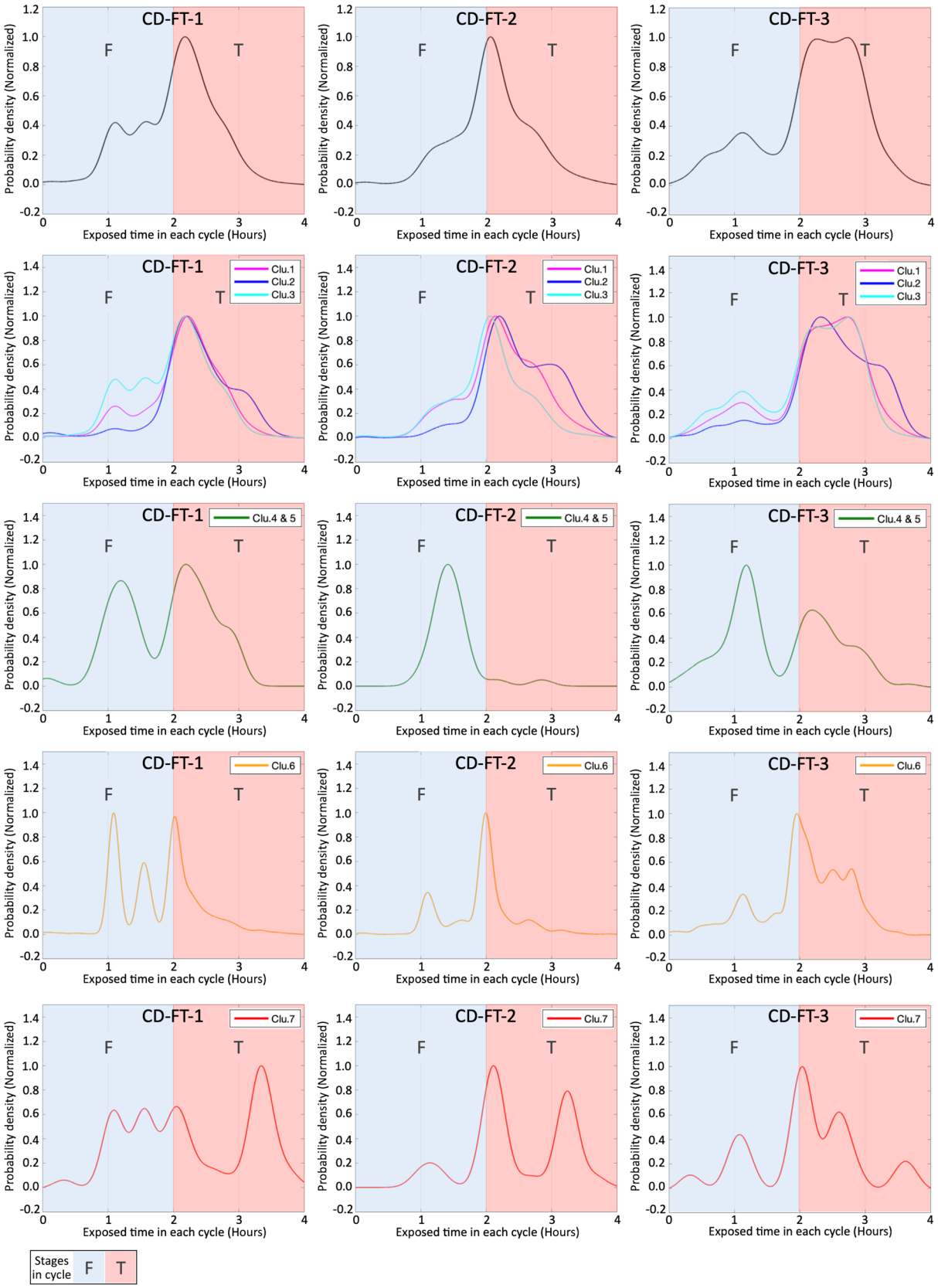

Fig. 16 The probability distribution for the monitored AE signals within a single cycle

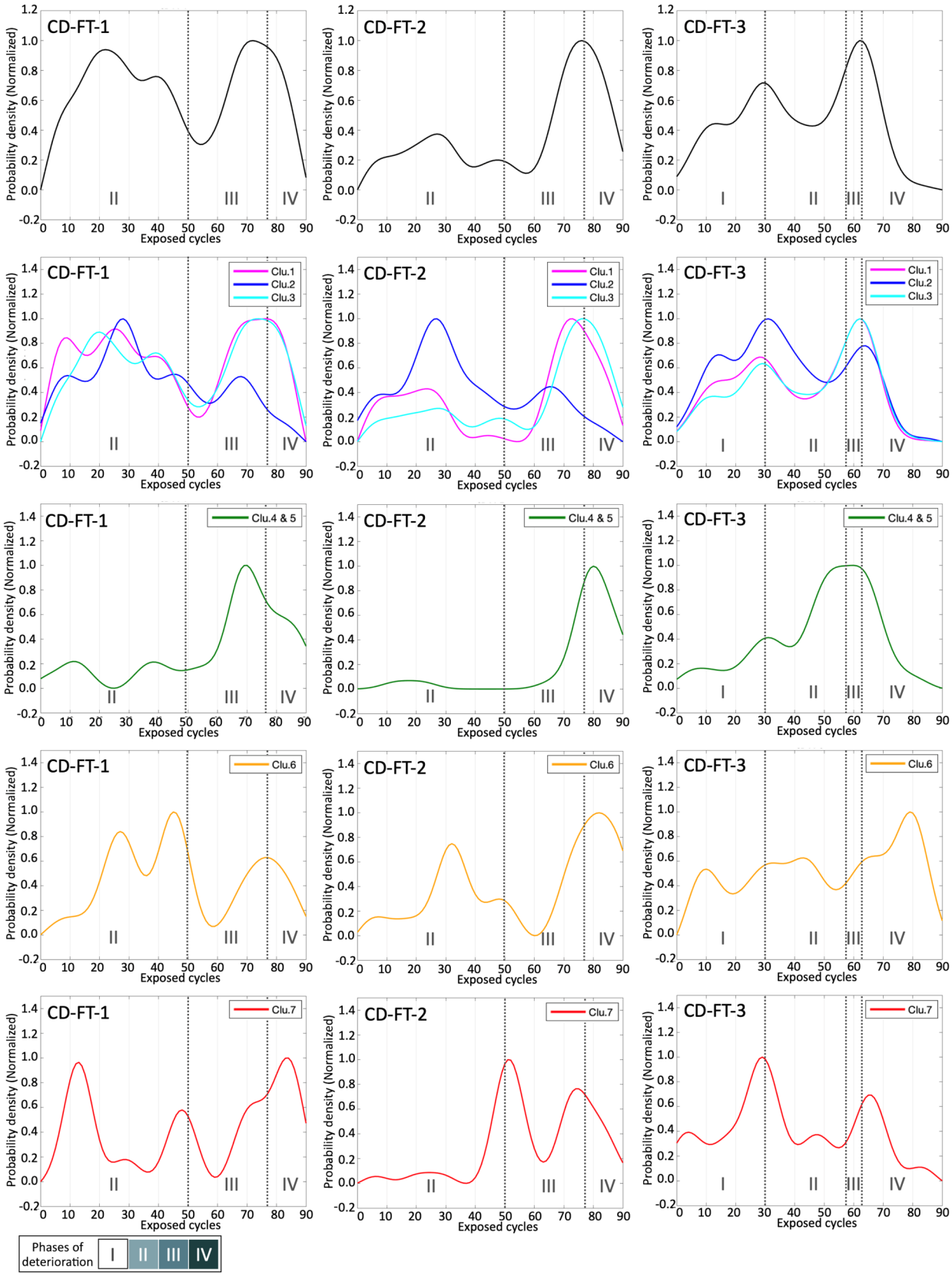

Fig. 17 The probability distribution for the monitored AE signals during the overall F–T deterioration process

probability distribution of the monitored AE signals during the entire deterioration process (Fig. 17) shows similar bimodal distributions corresponding to the deterioration phases defined by macroscopic morphological changes and P-wave velocity. There is a significant peak in phase III and another in the earlier phases (phase II for CD-FT-1 and CD-FT-2 and phases I and II for CD-FT-3). Among the clusters, Cluster 2 is more pronounced around phases I and II, while Clu. 4 and 5 show prominent peaks around phases III and IV. In contrast, both Clu. 6 and 7 are more likely described as multimodal distributions with relatively noticeable peaks around phases I, II and IV, except for phase III.

Signal features in connection with the deterioration phases

F–T deterioration of stone is generally attributed to the crystallization pressures that occur when the temperature has dropped sufficiently low to enable ice growth in pores; the pore wall provides a counterpressure to prevent a crystal from growing larger than the pore [28]. Once the total pressure exceeds the local tensile strength of the stone, damage will be preferentially generated at strength defects, such as granular disintegration at grain boundaries, as microscopic cracks invisible to the naked eye below the surface. Within subsequent F–T cycles, ice will preferentially nucleate within the cracks, inducing more microcracks, and the cracks progressively widen during the freezing stages but close again during the thawing stages [29]. This finding likely corresponds to deterioration phases I and II of this study. Once a critical number of microcracks are developed, the deterioration will progress rapidly over a short number of F–T cycles, showing significant surface damage [30]. This was observed in deterioration phase III of this study.

The possible distributions of the overall monitored AE signals show that the highest activity of AE events likely occurs in the early phase of the fast escalation in surface temperature within the thawing stage and phase III of deterioration with a rapid increase in the number, width and length of cracks. Notably, CD-FT-3, which exhibits more complete four deterioration phases, shows bimodal distributions with peaks in earlier phases (other than phase III) before the first surface crack has been revealed. These results validate the applicability of AE in monitoring the F–T deterioration process of stone and early warning prior to discernable damage.

The clustering results imply that signals with certain characteristics are more likely to occur in certain deterioration phases, which can be applied as indicators in deterioration monitoring.

Clu. 4 and 5, which present significantly higher ABE (3.5E+04 − 3.1E+06) along with low RA values, AF and PF, prefer to occur in the freezing stage and phases III and IV. This may implicate the sudden redistribution of stored strain energy in propagating cracks to the outer layer.

Clu. 6, which presents a moderate ABE (3.2E+00 − 1.7E+05), RA value (5.0 – 38.8), PF (1 – 483) and low AF (2 – 77), and Clu. 7, which presents a greater RA value (32.4 – 148.9), moderate ABE (7.8E+00 − 3.9E+04), low AF (3 – 27), and PF (11 – 297), are both likely to occur in phases I, II and IV. Clu. 6 prefers the freezing stages, and Clu. 7 prefers the thawing stages. A higher RA value represents AE signals with longer R and D and a lower A, which is usually attributed to deformation and shear crack propagation in materials. Clu. 6 and 7 of earlier deterioration phases may be related to the opening/closing of microcracks accompanied by the growth/thawing of ice crystals within the F–T cycle. In phase IV, this may be attributed to the deformations and frictions among the cross-cutting cracks caused by the displacement of crack surfaces along with the growth/melt of ice.

Clu. 2, which presents a higher PF (60 – 495), moderate AF (0 – 1167) and ABE (0.0E+00 − 6.0E+04), along with a low RA value (0.0 – 10.7), preferentially occurs in the thawing stage, and phases I and II may implicate the release of stress introduced by thawing ice crystals in the pores and microcracks of the stone matrix. The literature on the F–T deterioration of concrete reports that the main PF of the AE signal in the earlier deterioration phase is up to 200 kHz and gradually decreases with increasing number of F–T cycles [31]. The PF is likely to decrease as deterioration proceeds.

Conclusion

In this research, a set of procedures and related methodology is proposed based on the AE waveform parameters for denoising, and the classification and characterization of monitored AE signals. The clustered AE signals present different temporal characteristics of the occurrence time within a single F–T cycle and the overall F–T deterioration process of 90 cycles. Signals with certain characteristics are more likely to occur at a particular deterioration phase. Signals characterized by the significant absolute energy (ABE) are presumed to be related to the propagation of cracks to the outer layer. Signals characterized by a higher indirect parameter RA value may connect with the opening/closing of microcracks in the earlier phase of the deterioration process prior to the exposure of visible surface cracks. The peak frequency (PF) is likely to decrease as the deterioration proceeds. These results provide some indicative parameters worthy

of further research for realizing long-term monitoring of the F–T deterioration process in practice.

The results of this study demonstrate the potential use of AE technology in tracking mechanical changes in stone materials undergoing deterioration, and provide clustering analysis as a promising approach to signal interpretation. Although to realize practical contributions of AE technology for stone monuments in actual monitoring applications in the future, further work is needed. It is inspired that the directions worth exploring should not be restricted to the monitoring of deterioration development but also extend to early warning and risk evaluation in overall conservation activities. For instance, effectiveness assessment and optimizations of conservation materials and treatments. Besides, it will also be very interesting to see how AE technology works in cooperation with other monitoring technologies.

In the work plan following this study, firstly, the source definition of AE signals and verification of their correlations with the deterioration process in the context of related existing achievements of deterioration mechanism research, rock mechanics, and rock failure tests are not just limited to tuff and F–T deterioration. Moreover, signal processing and classification approaches are essential for improvements to determine the deterioration type and progression stage by AE signal analysis, in combination with field experiments.

Acknowledgements
We would like to acknowledge our colleagues, Dr. Mingshen Shao, Jianhui Liu, Dr. Weichang Chen, and Dong Xu (China Academy of Cultural Heritage), for their kind encouragement and warm-hearted assistance in the conceptualization, specimens preparation, and experimental design of this study, and writing of this paper.

Author contributions
Conceptualization, Y.Z., L.L., Y.L., Z.Z. and T.M.; methodology, Y.Z., Y.L., and T.M.; validation, Y.Z. and Y.L.; formal analysis, Y.Z.; investigation, Y.Z.; resources, Y.Z.; data curation, Y.Z.; writing—original draft preparation, Y.Z.; writing—review and editing, Y.Z., L.L.; visualization, Y.Z.; supervision, L.L., Z.Z. and T.M.; project administration, Y.Z. All authors have read and agreed to the published version of the manuscript. All authors read and approved the final manuscript.

Funding
This research received funding from "Special Funds for Basic Research of Central Public Welfare Research Institutes" of the China Academy of Cultural Heritage (No. 2021-JBKY10, No. 2023-JBKY-06), "Grant-in-Aid for Research Activity Start-up" of Japan Society for the Promotion of Science (No. 19K23100), the National Key Research and Development Program of China (No. 2019YFC1520600), Science and Technology Program of Gansu Province (No. 20JR5RA053).

Availability of data and materials
Not applicable.

Declarations

Competing interests
Not applicable.

Received: 20 December 2022 Accepted: 26 May 2023
Published online: 07 June 2023

References

1. Siegesmund S, Snethlage R. Stone in architecture: properties, durability. 4th ed. Springer: Berlin; 2011.
2. Suzuki T. 1 - Damage evaluation in concrete materials by acoustic emission. In: Ohtsu M, editor. Acoustic emission and related non-destructive evaluation techniques in the fracture mechanics of concrete. Oxford: Woodhead Publishing; 2015. p. 1–14.
3. Acoustic Emission Monitoring for Cultural Heritage. Getty Conservation Institute: Los Angeles, 2020. http://hdl.handle.net/10020/gci_pubs/acoustic_emission.Accessed on 1 Nov 2022.
4. Grossi C, Esbert R, Rio LSD, Montoto M, Laurenzi-Tabasso M. Acoustic emission monitoring to study sodium sulphate crystallization in monumental porous carbonate stones. Stud Conserv. 1997;42(2):115–25.
5. Strojecki M, Łukomski M, Krzemień L, Sobczyk J, Bratasz Ł. Acoustic emission monitoring of an eighteenth-century wardrobe to support a strategy for indoor climate management. Stud Conserv. 2014;59(4):225–32.
6. Łukomski M, Beltran V, Boersma F, Druzik J, Freeman A, Strojecki M, Learner T, Taylor J. Monitoring acoustic emission in an epidemiological pilot study of a collection of wooden objects. Stud Conserv. 2018;63:181–6. https://doi.org/10.1080/00393630.2018.1471892.
7. Strivens TA. The application of acoustic emission to the study of paint failure. J Oil Colour Chem Assoc. 1980;63(10):412–8.
8. Crawley EF, de Luis J. Use of piezoelectric actuators as elements of intelligent structures. AIAA J. 1987;25:1373–85. https://doi.org/10.2514/3.9792.
9. Ohtsu M, Isoda T, Tomoda Y. Acoustic emission techniques standardized for concrete structures. J Acoust Emission. 2007;25(2007):21–32. https://www.ndt.net/article/jae/papers/25-021.pdf. Accessed 1 Nov 2011
10. Rilem-Technical-Committee. Recommendation of RILEM TC 212-ACD: acoustic emission and related NDE techniques for crack detection and damage evaluation in concrete. Mater Struct. 2010;43:1183–6. https://doi.org/10.1617/s11527-010-9639-z.
11. Calabrese L, Proverbio E. A review on the applications of acoustic emission technique in the study of stress corrosion cracking. Corros Mater Degrad. 2021;2:1–30.
12. Mistras Group. PCI-2 based AE system 1 user's manual. Physical Acoustics Corporation, Princeton Junction, NJ,USA. 2007. p. 29–34.
13. Saliba J, Loukili A, Grondin F. 6 - Acoustic emission monitoring and quantitative evaluation of damage in concrete beams under creep. In: Ohtsu M, editor. Acoustic emission and related non-destructive evaluation techniques in the fracture mechanics of concrete. Oxford: Woodhead Publishing; 2015. p. 113–36.
14. Proverbio E, Calabrese L. 12 - Artificial neural network analysis of acoustic emission data during longtime corrosion monitoring of post-tensioned concrete structures. In: Ohtsu M, editor. Acoustic emission and related non-destructive evaluation techniques in the fracture mechanics of concrete. Oxford: Woodhead Publishing; 2015. p. 237–67.
15. ICOMOS-ISCS. Illustrated glossary on stone deterioration patterns. 2008, 86.
16. Li, L.; Chen, W.; Shao, M. Tuff rocks diseases mechanism analysis and preservation in Chengde Mountain Resort. In Proceedings of the Ancient Underground Opening and Preservation: Proceedings of the International Symposium on Scientific Problems and Long-term Preservation of Large-scale Ancient Underground Engineering Longyou, Zhejiang, China, 2015; pp. 101–109.
17. International Organization for Standardization. Hygrothermal performance of building materials and products — Determination of water absorption coefficient by partial immersion. **2016**, *BS EN ISO 15148: 2002 +A1:2016*. https://www.iso.org/standard/67183.html.
18. Ghobadi MH, Taleb Beydokhti AR, Nikudel MR, Asiabanha A, Karakus M. The effect of freeze–thaw process on the physical and mechanical properties of tuff. Environ Earth Sci. 2016;75:846. https://doi.org/10.1007/s12665-016-5664-8.
19. Nazarchuk Z, Skalskyi V, Serhiyenko O. Acoustic emission: methodology and application. Cham: Springer; 2016.

20. Ohtsu M. Introduction In acoustic emission and related non-destructive evaluation techniques in the fracture mechanics of concrete. In: Ohtsu M, editor. Introduciton. Oxford: Woodhead Publishing; 2015.
21. Saliba J, Loukili A, Grondin F, Regoin JP. Identification of damage mechanisms in concrete under high level creep by the acoustic emission technique. Mater Struct. 2013. https://doi.org/10.1617/s11527-013-0113-6.
22. Hierarchical Clustering - MATLAB & Simulink - MathWorks: https://ww2.mathworks.cn/help/stats/hierarchical-clustering.html#bq_679x-11. Accessed 1 Nov 2022.
23. kmeans - MATLAB & Simulink - MathWorks. https://ww2.mathworks.cn/help/stats/kmeans.html?searchHighlight=k-means%20clustering&s_tid=srchtitle_k-means%2520clustering_2#buefthh-3. Accessed 1 Nov 2022
24. SilhouetteEvaluation - MATLAB & Simulink - MathWorks. https://ww2.mathworks.cn/help/stats/clustering.evaluation.silhouetteevaluation.html. Accessed 1 Nov 2022.
25. Arima S, Isimura S. The story of multivariate analysis (Tahennryou Kaiseki No Hanasi). Tokyo: TokyoTosho Co.,Ltd. 2000.
26. Hall K. Rock moisture content in the field and the laboratory and its relationship to mechanical weathering studies. Earth Surf Proc Land. 1986;11:131–42. https://doi.org/10.1002/esp.3290110204.
27. Sicakova A, Draganovska M, Kovac M. Water absorption coefficient as a performance characteristic of building mixes containing fine particles of selected recycled materials. Procedia Engineering. 2017;180:1256–65. https://doi.org/10.1016/j.proeng.2017.04.287.
28. Deprez M, Kock TD, Schutter GD, Cnudde V. A review on freeze-thaw action and weathering of rocks. Earth-Sci Rev. 2020;203:103143. https://doi.org/10.1016/j.earscirev.2020.103143.
29. De Kock T, Boone MA, De Schryver T, Van Stappen J, Derluyn H, Masschaele B, De Schutter G, Cnudde V. A pore-scale study of fracture dynamics in rock using X-ray micro-CT under ambient freeze-thaw cycling. Environ Sci Technol. 2015;49:2867–74. https://doi.org/10.1021/es505738d.
30. Martínez-Martínez J, Benavente D, Gomez-Heras M, Marco-Castaño L, García-del-Cura MÁ. Non-linear decay of building stones during freeze–thaw weathering processes. Constr Build Mater. 2013;38:443–54. https://doi.org/10.1016/j.conbuildmat.2012.07.059.
31. Topolář L, Kocáb D, Pazdera L, Vymazal T. Analysis of acoustic emission signals recorded during freeze-thaw cycling of concrete. Materials. 2021. https://doi.org/10.3390/ma14051230.

Publisher's Note